Biophysical Journal
Article

Biophysical Society

MMP Secretion Rate and Inter-invadopodia Spacing Collectively Govern Cancer Invasiveness

Sandeep Kumar,[1] Alakesh Das,[1] Amlan Barai,[1] and Shamik Sen[1,*]
[1]Department of Biosciences and Bioengineering, Indian Institute of Technology Bombay, Mumbai, India

ABSTRACT Invadopodia are micron-sized invasive structures that mediate extracellular matrix (ECM) degradation through a combination of membrane-bound and soluble matrix metalloproteinases (MMPs). However, how such localized degradation is converted into pores big enough for cancer cells to invade, and the relative contributions of membrane-bound versus soluble MMPs to this process remain unclear. In this article, we address these questions by combining experiments and simulations. We show that in MDA-MB-231 cells, an increase in ECM density enhances invadopodia-mediated ECM degradation and decreases inter-invadopodia spacing. ECM degradation is mostly mediated by soluble MMPs, which are activated by membrane-bound MT1-MMP. We present a computational model of invadopodia-mediated ECM degradation, which recapitulates the above observations and identifies MMP secretion rate as an important regulator of invadopodia stability. Simulations with multiple invadopodia suggest that inter-invadopodia spacing and MMP secretion rate collectively dictate the size of the degraded zones. Taken together, our results suggest that for creating pores conducive for cancer invasion, cells must tune inter-invadopodia spacing and MMP secretion rate in an ECM density-dependent manner, thereby striking a balance between invadopodia penetration and ECM degradation.

INTRODUCTION

Cancer metastasis, the leading cause of cancer mortality, involves the escape of cancer cells from the primary tumor and their invasion into distant tissues (1,2). Invadopodia are micron-sized, actin-rich, subcellular structures that are associated with extracellular matrix (ECM) degradation, and have been implicated in cancer invasion and metastasis (3–5). On two-dimensional substrates coated with ECM ligands, invadopodia are manifested as small, actin-rich dots that protrude into their underlying matrix and colocalize with several classes of proteins, including adhesion proteins, actin-associated proteins, and ECM-degrading proteinases (5–7). Matrix metalloproteinases (MMPs)—one of the major ECM-degrading enzymes that mediate invasion (8,9)—can broadly be classified into membrane-anchored MMPs (e.g., MT1-MMP) and soluble MMPs (e.g., MMP2, MMP9). Although MT1-MMP remains attached to the invadopodia tip and causes localized degradation, it also activates soluble MMPs secreted by the invadopodia (10). The activated soluble MMPs diffuse into the extracellular space and mediate ECM degradation, both in the neighborhood of the invadopodia as well as far away (11–13).

Recent studies have revealed that invadopodia dynamics is strongly influenced by both intrinsic cell properties such as cell contractility, as well as mechanical context provided by the ECM (14–16). In a landmark study, Weaver and co-workers (17) demonstrated that higher ECM stiffness drives enhanced ECM degradation through increased invadopodia formation and higher invadopodia activity. In a follow-up study, the same group demonstrated the ability of invadopodia to sense a wide range of ECM stiffness (14). Given the prominent role of integrins in ECM stiffness-sensing, integrin signaling is expected to play important role in regulating invadopodia dynamics. Indeed, integrins have been shown to directly influence invadopodia formation, stability, and activity (18–20). Further, $\alpha5\beta1$ integrins have been demonstrated to act as docking proteins for seprase to form functional invadopodia (21). Although these studies have contributed to our understanding of invadopodia dynamics, several questions related to the structure and working of invadopodia remain unanswered. For example, although both soluble MMPs and membrane-anchored MMPs have been implicated in ECM degradation, their individual contributions to ECM degradation remain unclear. Further, although multiple invadopodia have been

Submitted January 23, 2017, and accepted for publication November 20, 2017.

*Correspondence: shamiks@iitb.ac.in
Sandeep Kumar and Alakesh Das contributed equally to this work.

Editor: Alissa Weaver.
https://doi.org/10.1016/j.bpj.2017.11.3777

observed on the cell surface, any dependence of invadopodia positioning on ECM properties and its potential implications have not been studied.

Computational modeling has provided several insights about various aspects of cancer invasion (22–25), including invadopodia dynamics. One of the first models of invadopodia-mediated ECM degradation was developed by Weaver and co-workers (26). Cellular automaton framework presented in this work accounted for feedback between invadopodia and matrix, and was able to reproduce the experimentally observed inhibitory effect of ECM cross-linking on invadopodia growth. In another study, Saitou et al. (27) used Monte Carlo simulations to computationally demonstrate the formation of finger-like projections that were comparable in size and lifetime to that of invadopodia. In addition to the concentration of MMPs, Ichikawa and co-workers (13) identified MMP turnover as an important factor in regulating invadopodia activity. In their follow-up work, the same group reported the existence of a temporary transient phase in MT1-MMP activity followed by steady state activity, with existence of the transient phase key to ECM degradation (28). Although these studies have indeed improved our understanding of invadopodia dynamics, several aspects of invadopodia have not been taken into account. For example, soluble MMP dynamics was not taken into account in the model developed by Weaver and co-workers (26). Further, given that cell-matrix adhesions stabilize invadopodia (18), it is likely that degradation kinetics of ECM surrounding invadopodia influence invadopodia stability and activity. However, this has not been adequately addressed.

In this article, we have combined experiments and computational modeling to gain insight into regulation of invadopodia-mediated ECM remodeling by MMPs. Using gelatin-coated substrates of varying densities but constant stiffness, we first demonstrate that an increase in ECM density drives ECM degradation through increased invadopodia activity. We then present a cellular automata (CA)-based, discrete computational model for studying the collective influence of ECM density and MMP secretion rate on ECM degradation, mediated by membrane-anchored MT1-MMP attached to the invadopodia tip and soluble MMPs secreted by the invadopodia. By choosing an ECM density-dependent MMP activity profile, we demonstrate that invadopodia speed and ECM degradation exhibit distinct sensitivities to MMP secretion rates. Our simulation, as well as experimental results, also suggest that although soluble MMPs play a major role in ECM degradation, MT1-MMP plays a major role in invadopodia penetration. Lastly, we probe the functional relevance of ECM density-dependent inter-invadopodia spacing. We show that moderate inter-invadopodia spacing leads to the fusion of the ECM degradation zones of neighboring invadopodia, thereby creating pores conducive to cell invasion. Taken together, our results suggest that inter-invadopodia spacing and MMP secretion rate collectively influence cell invasiveness.

MATERIALS AND METHODS

Experimental methods: cell culture

MDA-MB-231 breast cancer cells were obtained from National Center for Cell Science (Pune, India) and cultured in high-glucose Dulbecco's Modified Eagle Medium (Invitrogen, Carlsbad, CA) containing 10% fetal bovine serum (Hi-media). Cells were maintained inside a CO_2 incubator (Thermo Scientific, Waltham, MA) at 37°C and a 5% CO_2 conditioned environment. Cell were maintained in 60 cm^2 culture dishes (Nest) and passaged when 80–90% confluent using 0.25% Trypsin-EDTA (Hi-media).

Experimental methods: gelatin degradation assay

For the degradation assay, 12 mm coverslips were first treated with 10 mg/mL poly-L-lysine (Sigma, St. Louis, MO) for 20 min. Then they were treated with 0.5% glutaraldehyde (Sigma) in H_2O for 30 min. After washing for three times with H_2O, coverslips were coated with fluorescent gelatin for degradation studies, as mentioned elsewhere (29). For fluorescence labeling, unlabeled 5.0 and 0.5% gelatin (cat. #2500, porcine origin; Sigma) in 1× phosphate buffered saline (PBS) was mixed with Oregon-Green 488 conjugated gelatin (cat. #G13186; Invitrogen) at 1:300 dilution. For degradation studies, cells were seeded at a density of 2×10^3 cells/cm^2 for 8–10 h; initially cells were allowed to adhere for 15–20 min, and then drugs were added at desired concentration. For inhibiting microvesicle-mediated ECM degradation, cells were treated with the Rho-ROCK inhibitor Y-27632 (cat. #CAS 146986-50-7, 1 μM; Calbiochem). SB-3CT (cat. #ab141579, 5 μM; Abcam, Cambridge, UK) was used for inhibiting proteolytic activity of soluble MMPs, whereas MT1-MMP-mediated ECM degradation was suppressed using NSC405020 (cat. #4902 50 μM; Tocris Bioscience). For inhibition of the catalytic domain of MT1-MMP necessary for activating soluble MMPs, MT1-MMP blocking antibody (cat. #ab78738 [LEM-2/63.1]; Abcam) was used at a concentration of 2 μg/mL (30,31).

Experimental methods: immunocytochemistry

For staining, cells were fixed with 4% paraformaldehyde (Sigma) prepared in 1× PBS for 20 min. After washing three times with 1× PBS, cells were permeabilized with 0.1% Triton X-100 in 1× PBS for 5–10 min under mild shaking. Subsequently, cells were blocked with 2% bovine serum albumin (BSA) (Merck, Kenilworth, NJ) for 45 min at room temperature (RT), and then incubated with anti-MT1-MMP mouse monoclonal antibody (cat. #ab78738; Abcam) overnight at 4°C. The next day, after washing three times with 1× PBS, cells were incubated with Alexa Fluor 647 conjugated anti-mouse immunoglobulin G (IgG) (cat. #A-21236; Invitrogen) at RT for 2 h. Then after washing three times with 1× PBS, coverslips were mounted onto glass slides using Eukitt quick-hardening mounting medium (Sigma). For quantification of the cell spread area, cells were stained using Alexa Fluor 555 conjugated phalloidin for 1 h at RT. Cells were imaged at 63× magnification using Scanning Probe Confocal Microscope (LSM 780; Zeiss, Oberkochen, Germany). Quantification of the degraded area per cell was performed by dividing the degraded area underneath each cell by the total cell spreading area (visualized using F-actin). For doing this, the cell boundary and the degraded matrix beneath each cell were thresholded, and the thresholded areas were determined using the ImageJ Analyze particle tool. For determining the number of invadopodia per cell, only the round F-actin punta colocalized with degraded spots were considered as invadopodia, as done elsewhere (18). The number of invadopodia per cell, invadopodia width, and inter-invadopodia spacing were manually obtained using the *freehand lines* tool of Fiji-ImageJ software. Further, inter-invadopodia spacing was calculated only for those cases where the distance was less than five times the invadopodia width (i.e., 5 μm). From MT1-MMP-stained images, the location of invadopodia was determined from the presence of MT1-MMP and F-actin overlapping intensity peaks ($\geq$0.5 μm width (32)) at the basal surface of the cell in contact with gelatin.

Experimental methods: Western blotting

For Western blotting, cells were lysed using radioimmunoprecipitation assay (RIPA) buffer (Sigma) containing a cocktail of protease and phosphatase inhibitors (Sigma). The protein concentration of cell lysates were determined using a Bradford assay. At least 20–30 μg of protein was loaded per condition. Proteins were separated using 12% sodium dodecyl sulphate-polyacrylamide gel electrophoresis (SDS-PAGE) and transferred onto 0.22 μm nitrocellulose membrane (PALL Life Sciences). After transfer, the membranes were blocked using 5% BSA in 1× Tris-buffered saline and Tween-20 (TBST) for 1 h at RT, and incubated with the primary antibodies anti-phospho-myosin light chain 2 (Thr18/Ser19) rabbit monoclonal antibody (cat. #3674; CST) and anti-β-actin antibody mouse monoclonal antibody (cat. #ab8226; Abcam), overnight at 4°C under mild shaking conditions. After washing three times with 1× TBST, membranes were incubated with the following secondary antibodies at RT for 1 h: horseradish peroxidase (HRP)-conjugated anti-rabbit IgG (Invitrogen) and HRP-conjugated anti-mouse IgG (Invitrogen). Subsequently, after washing three times with 1× TBST, blots were developed in x-ray films (Kodak, Rochester, NY) using a chemiluminescent ECL kit (Pierce).

Experimental methods: statistics

Statistical data was first tested for normality using the Kolmogorov-Smirnov normality test. For parametric data, statistical analysis was performed using one-way ANOVA/two-way ANOVA, with the Fisher post-hoc test used to compare the means. For nonparametric data, the Mann-Whitney test was performed. All statistical analyses were performed using Origin 9.1, with $p < 0.05$ considered to be statistically significant.

Computational model construction and parameter values

The model of invadopodia was constructed by integrating a three-dimensional (3D) CA-based discrete model with reaction diffusion dynamics. Although invadopodia penetration, MT1-MMP activity, MMP secretion, and ECM degradation were modeled using CA-based modeling, diffusion and degradation activities of soluble MMPs were modeled using reaction-diffusion dynamics. Simulation parameters were either taken from the literature, or determined based on experimental observations. Although soluble MMP secretion rate, diffusion coefficient, and degradation rate were taken from previously published work (12,27), invadopodia width and inter-invadopodia spacing were decided based on our experimental observations. Since invadopodia can be longer than 2 μm (32), invadopodia were allowed to penetrate up to 4 μm in our simulations. Further, one lattice pixel was assumed to be $200 \times 200 \times 200$ nm^3 and one simulation step was assumed to be 1 s. Other parameters, including secretion/degradation rate and diffusion coefficient rate of MMPs, were scaled accordingly. Also, to account for the fact that invadopodia have a lifetime of $\sim$1 h, invadopodia growth was simulated for a maximum of 3600 simulation steps. MMP secretion rate and ECM density were varied in our simulations to probe their role in ECM degradation and invadopodia penetration. Lastly, inter-invadopodia spacing was also varied in one set of simulations.

Computational model implementation, data visualization, and analysis

The multiscale simulation package CompuCell3D (33) was used to implement the present model. Because we used CA-based modeling, the plugin section of the CompuCell3D simulation engine, which implements the cellular potts modeling algorithm, was not used in our study. All the CA rules were implemented using custom steppables. Python-based custom steppables were written to implement invadopodia penetration, MMP secretion, ECM degradation, and for data logging. Reaction-diffusion dynamics of MMP molecules was implemented using the already available "DiffusionSolverFE" steppable. *.csv data files were generated through simulation code (data logging steppable) and were processed using custom-written MATLAB scripts to quantify different metrics, including ECM degradation, invadopodia speed, and MMP secretion. Additionally, *.vtk files were also generated from simulations and were used for 3D visualization in ParaView (34). Lastly, pore size of the degraded area was quantified using ImageJ.

RESULTS

Increase in ECM density enhances invadopodia-mediated ECM degradation

To probe the influence of ECM density on invadopodia-mediated ECM degradation, experiments were performed by culturing MDA-MB-231 breast cancer cells on glass coverslips coated with fluorescence-labeled gelatin at concentrations of 0.5 and 5.0%, respectively (Fig. S1 *A*). Since ECM stiffness regulates invadopodia activity (17) and our aim was to study the role of ECM density on invadopodia activity, the thickness of the gelatin matrices was intentionally kept very low ($\approx 1\mu$m) (Fig. S1 *B*). Since cells can sense several microns into their surrounding microenvironment (35,36), and our thin matrices were fabricated on glass substrates, it is likely that cells were sensing the rigid glass coverslips. Using a spherical AFM probe, the effective stiffness of both 0.5 and 5.0% gelatin substrates was estimated to be $\approx$40 kPa (Fig. S1 *C*). Given that both the thickness and the stiffness of these substrates were nearly the same, any differences in invadopodia number and/or their activity observed in our experiments can be attributed to differences in ECM density.

ECM degradation is mediated not only by invadopodia, but also by cell secreted microvesicles (37–39). Although both Rho-ROCK (40) and Rac-p38 MAPK pathways (41,42) have been shown to regulate invadopodia activity, microvesicle secretion is positively regulated by the Rho-ROCK pathway (43,44). Given the mutually antagonistic relationship between Rho and Rac GTPases (45), inhibition of Rho may not only inhibit microvesicle secretion, but may also promote invadopodia activity through Rac activation (44). In addition, Src homolog domain-containing phosphatase 2 was found to promote invadopodia activity via suppression of Rho signaling in multiple types of cancer cells, including MDA-MB-231 cells (46). Therefore, to probe the individual contribution of invadopodia in mediating ECM degradation, microvesicle-mediated ECM degradation was blocked using the ROCK inhibitor Y-27632, which inhibits phosphorylation of myosin light chain (Fig. 1 *A*). Dose-dependent studies revealed that a 1 μM drug concentration was sufficient to suppress $\approx$90% of phosphorylation of myosin light chain activity (Fig. 1 *B*). Hence, all subsequent experiments were performed at this dose.

ECM degradation was quantified by dividing the degraded area underneath each cell by the total cell spread

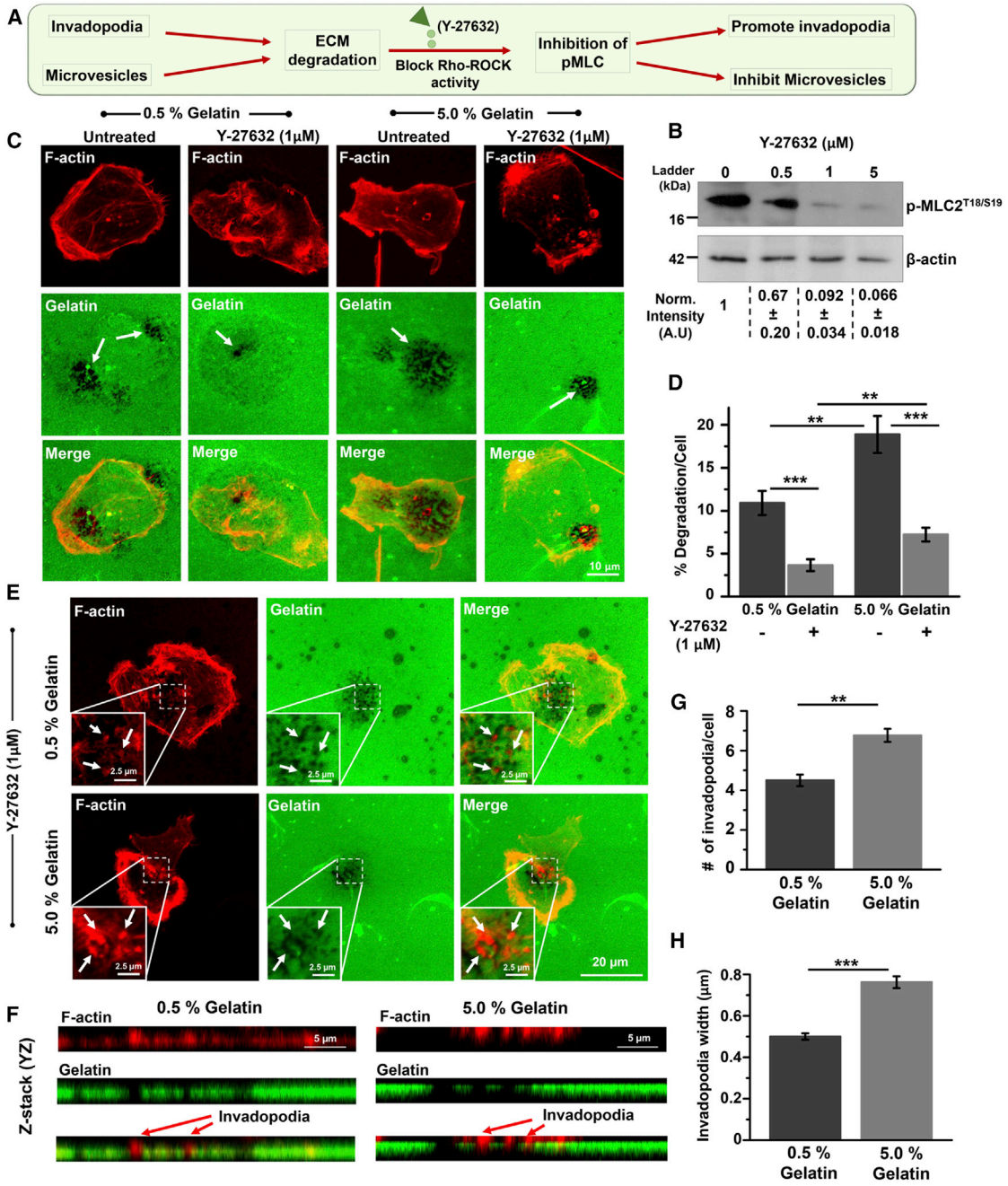

FIGURE 1 Influence of ligand density on ECM degradation and invadopodia in MDA-MBA-231 breast cancer cells. (*A*) Schematic of ECM degradation by invadopodia and microvesicles. (*B*) Western blot showing dose-dependent regulation of p-MLC2$^{T18/S19}$ in MDA-MB-231 cells upon treatment with the Rho-ROCK inhibitor Y-27632. β-actin served as a loading control. Densitometric quantification of immunoblots revealed downregulation of p-MLC2$^{T18/S19}$ with an increase in dosage of Y-27632 ($n = 2$). Error bars show standard deviation. (*C*) Representative images of ECM degradation in untreated and 1 μM Y-27632-treated MDA-MB-231 cells cultured on 0.5 and 5.0% gelatin-coated substrates. White arrows indicate degraded area. Scale bar represents 10 μm. (*D*) Quantification of percentage degradation/cell in untreated and Y-27632-treated cells cultured on 0.5 and 5.0% gelatin-coated substrates. Statistical significance was performed using two-way ANOVA ($n = 2$, 25–30 cells per condition; $^{**}p < 0.01$, $^{***}p < 0.001$). Error bars show mean $\pm$ SE. (*E*) Representative images of invadopodia-mediated ECM degradation in untreated and 1 μM Y-27632-treated MDA-MB-231 cells cultured on 0.5 and 5.0% gelatin-coated substrates. Insets show colocalization of F-actin puncta and degraded areas. Scale bar represents 2.5 μm. Colocalization of actin puncta with degraded areas (*white arrows*) were considered as invadopodia. Scale bar represents 20 μm. (*F*) Representative confocal *z*-stack images (*YZ plane*) of Y-27632-treated cells cultured on 0.5 and 5.0% fluorescent gelatin. Cells were stained for F-actin (shown in *red*) and gelatin (shown in *green*). Scale bar represents 5 μm. Red arrows indicate colocalization of F-actin puncta (*invadopodia*) with degraded matrix. (*G*) Quantification of number of invadopodia/cell in cells cultured on 0.5 and 5.0% gelatin-coated substrates. Statistical significance was performed using one-way ANOVA ($n = 2$, 25–30 cells per condition; $^{**}p < 0.01$). Error bars show mean $\pm$ SE. (*H*) Quantification of invadopodia width in cells cultured on 0.5% and 5.0% gelatin-coated substrates. Statistical significance was performed using Mann-Whitney test ($n = 2$, 25–30 cells per condition; $^{***}p < 0.001$). Error bars show mean $\pm$ SE. To see this figure in color, go online.

area (Fig. 1, *C* and *D*). In the absence of Y-27632, an increase in ECM density led to a two-fold increase in ECM degradation from ~10% degradation observed on 0.5% gelatin density surfaces to ~20% degradation on 5.0% surfaces. Inhibition of microvesicle-mediated ECM degradation using Y-27632 led to a dramatic drop of ~60–70% in the extent of ECM degradation. However, in line with the study by Tsai et al. (46), Y-27632 treatment led to increase in the number of invadopodia per cell both on 0.5 and 5.0% gelatin-coated substrates (Fig. S2). The residual ECM degradation, mediated by invadopodia, increased from 3 on 0.5% gelatin-coated substrates to 7 on 5% gelatin-coated substrates. To determine if this increase in ECM degradation can be attributed to higher number of invadopodia and/or their activity, the average number of invadopodia per cell was quantified (Fig. 1, *E* and *F*). Quantification indeed revealed that an increase in ligand density led to an increase in the number of invadopodia per cell (Fig. 1 *G*). Additionally, invadopodia observed on 5.0% gelatin-coated substrates were 60% larger in width compared with those formed on 0.5% gelatin-coated substrates (Fig. 1 *H*). Together, these results suggest that an increase in ECM density promotes invadopodia-mediated ECM degradation through formation of a greater number and larger size of invadopodia.

Computational model of invadopodia reproduces experimental observations

To better understand how ECM density regulates invadopodia dynamics, a cellular automaton model was developed wherein a cell sits on top of a $5 \times 5 \times 5\ \mu m^3$ 3D ECM, and invadopodia penetrate into the underlying ECM (Fig. 2 *A*). The ECM was represented by a 3D cellular automaton of dimension in which higher order ECM elements were placed homogeneously, with one lattice unit

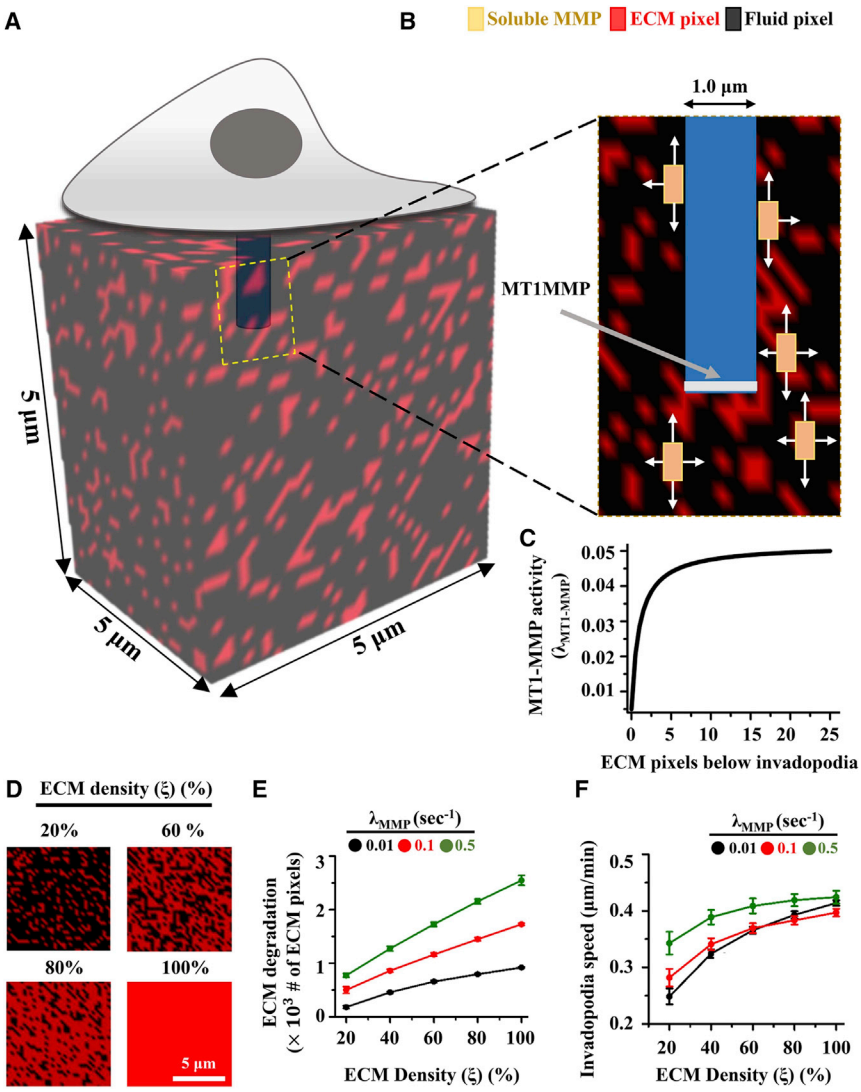

FIGURE 2 Computational model of invadopodia. (*A*) Invadopodium penetrates into a 3D ECM matrix of size $5 \times 5 \times 5\ \mu m^3$ with red pixels representing the ECM and black pixels representing free space. (*B*) MT1-MMP (*white*) remains localized at the tip of the invadopodia. Soluble MMPs secreted by the invadopodia diffuse into the extracellular space and degrade the ECM (*white arrows*). (*C*) Dependence of MT1-MMP activity level $0 \leq \lambda_{MT1\text{-}MMP} \leq 1$ on the total number of ECM sites in contact with the tip of the invadopodia. (*D*) ECM density was varied by varying the fraction of total simulation lattice covered by ECM pixels. Red: ECM site. Black: Fluid or ECM-free space. (*E* and *F*) Quantification of ECM degradation and invadopodia speed for varying values of ECM density at three different soluble MMP secretion rates, i.e., $\lambda_{MMP} = 0.01$, 0.1, and 0.5 s^{-1}. At least 50 simulations per condition were performed. Error bars are ± standard deviation. To see this figure in color, go online.

representing a volume of $200 \times 200 \times 200$ nm^3. Based on our experimental observations (Fig. 1 *H*), invadopodia width was set to 1 μm (Fig. 2 *B*). Invadopodia penetration into the matrix was affected by degradation of ECM sites by membrane-anchored MMPs (i.e., MT1-MMP) and soluble MMPs. No distinction was made between individual soluble MMPs (e.g., MMP2, MMP9, etc.). MT1-MMP was assumed to be localized at the moving front of the growing invadopodia (*white region* in Fig. 2 *B*). To model MT1-MMP-mediated ECM degradation at every simulation step, ECM degradation was performed below the invadopodia surface (discussed below). Since the size of a single pixel is far greater than the size of a single soluble MMP molecule, instead of modeling the dynamics of a single soluble MMP molecule, a soluble MMP concentration ([MMP]) was associated with each lattice site. To mimic experimentally observed ECM density-dependent MMP secretion (15,25), soluble MMPs were secreted by the invadopodia randomly along its surface based on the total number of ECM units in contact with the invadopodia ($N_{\mathrm{ECM,contact}}$). The total number of soluble MMPs secreted, $N_{\mathrm{MMPSecreted}}$, is given by the expression

$$N_{\mathrm{MMPSecreted}} = \lambda_{\mathrm{MMP}} \times N_{\mathrm{ECM,contact}}, \quad (1)$$

where λ_{MMP} represents the MMP secretion rate. λ_{MMP} was varied in our simulations to mimic the behavior of different cell types possessing different MMP activity. Diffusion and degradation of soluble MMPs were incorporated in our model using the reaction diffusion formalism given by Eq. 2:

$$\frac{\partial \mathrm{MMP}(\mathbf{x},t)}{\partial t} = D.\nabla^2 \mathrm{MMP}(\mathbf{x},t) - \delta \times \mathrm{MMP}(\mathbf{x},t), \quad (2)$$

where, $\mathrm{MMP}(\mathbf{x},t)$ represents the concentration of MMP molecules at point $\mathbf{x}$ and time t, and D and δ represent the diffusion coefficient and the degradation rate of soluble MMPs, respectively. The diffusion coefficient was chosen to be $D = 0.5 \times 10^{-9}$ cm^2/s^{-1}, comparable with reported values (12). The value of degradation rate, $\delta = 0.002$ s^{-1}, was taken from the literature (27).

At every step of the simulations ($\sim$1 s, see Materials and Methods), in the absence of any ECM below the invadopodia, the tip of the invadopodia was advanced by one step in downward direction. Else, ECM density ($[ECMDensity]$) of every ECM site below the invadopodia was decreased by the ECM density-dependent MT1-MMP activity level ($\lambda_{MT1-MMP}$) given by the expression

$$\lambda_{\mathrm{MT1\text{-}MMP}} = 0.005 + 0.0468\frac{N_{f,b}}{N_{f,b}+1}, \quad (3)$$

where $N_{f,b}$ represents the number of ECM fibers below the invadopodia. In this equation, the prefactor 0.0468 was used so as to have the maximum MMP activity of 0.05 corresponding to all sites below the invadopodia being occupied (i.e., $N_{f,b} = 25$) (Fig. 2 *C*). In this model, there exists no explicit mathematical equation connecting MT1-MMP and soluble MMP dynamics. However, soluble MMPs and MT1-MMP indirectly influence one another. First, MT1-MMP-mediated degradation of the ECM underneath the invadopodia leads to increase in invadopodia height and a corresponding increase in invadopodia-ECM contact. This in turn leads to higher soluble MMP secretion (Eq. 1). Second, as the invadopodia penetrates, degradation of the ECM below the invadopodia by soluble MMPs leads to a drop in MT1-MMP activity (Eq. 3).

To study the influence of ECM density on invadopodia growth, simulations of invadopodia penetration into 3D ECM matrices was performed at varying ECM densities ($\xi \in [20, 100]\%$). ξ was varied by varying the fraction of simulation lattice covered by ECM pixels (Fig. 2 *D*). Invadopodia was initially placed at the top of simulation lattice and allowed to penetrate into the ECM until it reached a maximum penetration depth of 5 μm (Movies S1 and S2). At least 50 simulations for each of the 15 scenarios (= for five different values of ξ $\times$ three different values of λ_{MMP}) were performed. At the end of each simulation, invadopodia activity was characterized by quantifying invadopodia penetration speed, ECM degradation, and the number of soluble MMPs secreted. In line with our experimental findings, an increase in ECM density enhanced ECM degradation (Fig. 2 *E*) through increased secretion of soluble MMPs (Fig. S3). Invadopodia speed increased modestly with an increase in ECM density, but did not vary significantly when secretion rate was varied from 0.01 to 0.5 s^{-1} (Fig. 2 *F*). In addition to reproducing our experimental observations, our results reveal differential sensitivities of ECM degradation and invadopodia speeds to ECM density and MMP secretion rates.

Differential contributions of MT1-MMP and soluble MMPs to ECM degradation and invadopodia penetration

Although an increase in MMP secretion rate does not appreciably influence invadopodia speed, it probably contributes to the extent of ECM degradation. To dissect the individual contributions of MT1-MMP and soluble MMP to ECM degradation, simulations were performed where the information on proteolysis performed by MT1-MMP and soluble MMPs were tracked individually (Fig. 3 A). To quantitatively assess the relative contributions of soluble and MT1-MMPs in mediating ECM degradation, at least 50 simulations per parameter combination were performed. Quantification suggests that although MT1-MMP-mediated proteolysis was responsible for $\sim$50% ECM degradation at the lowest MMP secretion rate (i.e., $\lambda = 0.01$ s^{-1}), the majority of the degradation (>75%) observed at the moderate and highest

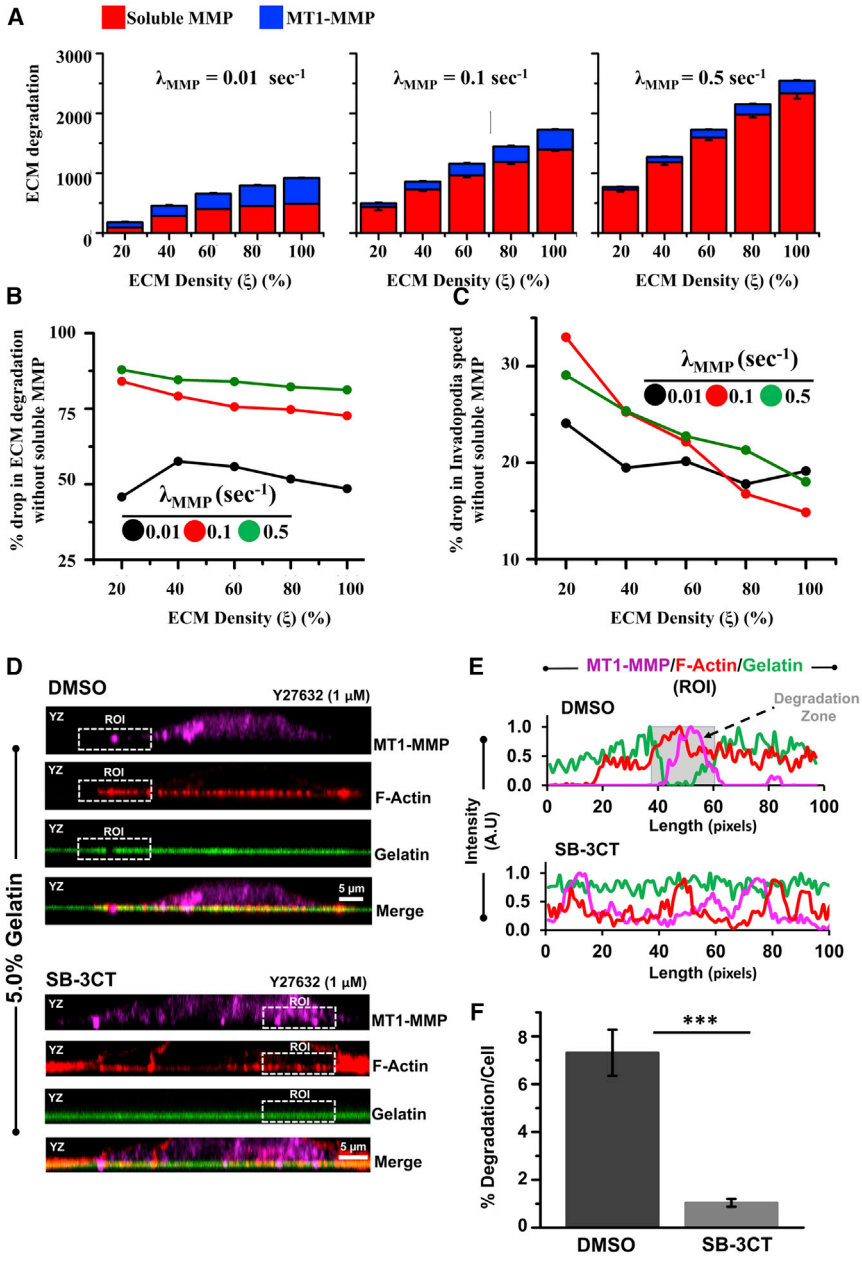

FIGURE 3 Contributions of soluble MMPs and MT1-MMP to ECM degradation and invadopodia speed. (*A*) ECM degradation by soluble MMPs (*red*) and MT1-MMP (*blue*) for three different soluble MMP secretion rates, i.e., $\lambda_{MMP} = 0.01$, 0.1, and 0.5 s^{-1}. At least 50 simulations per condition were performed. Error bars are ± standard deviation. (*B* and *C*) Percentage drop in ECM degradation (*B*) and invadopodia speed (*C*) upon inhibition of soluble MMPs, i.e., upon setting $\lambda_{MMP} = 0$. (*D*) Representative confocal *z*-stack immunostained images (in *YZ* plane) of DMSO and SB-3CT-treated MDA-MB-231 cancer cells cultured on 5.0% gelatin in the presence of 1 μM Y-27632. For localization of invadopodia, colocalized immunostained images of MT1-MMP and F-actin (≥0.5 μm wide) inside the fluorescent gelatin matrix were considered as invadopodia. Scale bar represents 5 μm. (*E*) Representative intensity profiles of MT1-MMP/F-actin/gelatin obtained from the zoomed images shown in insets (region of interest). Gray zone indicates the location of the degraded gelatin matrix in DMSO-treated MDA-MB-231 cancer cells. (*F*) Quantification of percentage degradation/cell in Y-27632-treated MDA-MB-231 cancer cells seeded on 5% gelatin in the presence of DMSO and SB-3CT. Statistical significance was performed using one-way ANOVA ($n = 2$, 25–30 cells per condition; $^{***}p < 0.001$). Error bars show mean ± SE. To see this figure in color, go online.

MMP secretion rates (i.e., $\lambda = 0.1$ and 0.5 s^{-1}) was mediated by soluble MMPs. Consistent with this, when soluble MMP activity was turned off (i.e., simulations were performed in the absence of soluble MMPs), ECM degradation dropped by ∼75% for $\lambda_{MMP} = 0.1$ and 0.5 s^{-1} (Figs. 3 *B* and S4 *A*). For the lowest MMP secretion rate (i.e., $\lambda_{MMP} = 0.1$), an ∼50% drop in ECM degradation was observed. In the absence of soluble MMPs, an ∼15–30% drop in invadopodia speed was observed (Figs. 3 *C* and S4 *B*), with the maximum drop observed at the lowest ECM density.

To compare these in silico results with experiments, degradation patterns were tracked on 5% gelatin-coated substrates in the presence and absence of the soluble MMP inhibitor SB-3CT, and in the presence of 1 μM Y-27632 (Fig. 3 *D*). Tracking of gelatin fluorescence intensity allowed us to assess the influence of SB-3CT on ECM degradation. Strikingly, SB-3CT treatment led to a dramatic decrease in ECM degradation from ∼7.5 to ∼0.75%, illustrating the robust contribution of soluble MMPs in mediating ECM degradation (Fig. 3, *E* and *F*). Since MT1-MMP is known to be the master regulator of soluble MMPs (47), experiments were performed in the presence of the MT1-MMP inhibitor NSC405020, as well as the blocking antibody that inhibits the catalytic domain of MT1-MMP associated with activating soluble MMPs. Under these conditions, ECM degradation was completely

abolished (Fig. S5), demonstrating the pivotal role of MT1-MMP in activating soluble MMPs. Collectively, these results suggest that although MT1-MMP plays a more dominant role in facilitating invadopodia penetration, ECM degradation is mainly performed by MT1-MMP-activated soluble MMPs.

Balancing ECM-mediated invadopodia stabilization and MMP secretion rates for optimizing ECM degradation and invadopodia penetration

In our model, we have assumed invadopodia penetration in the absence of ECM below the invadopodia. Although this may be true at the initial stages of invadopodia growth, as the invadopodia becomes larger in length, the aspect ratio (length/width ratio) increases dramatically, making it less stable. Under these conditions, lateral support provided by the ECM fibers may help in stabilizing the invadopodia. Adhesion rings surrounding invadopodia may provide such structural support (18,48). To study the consequence(s)/importance of such a regulatory mechanism on invadopodia growth and subsequent ECM degradation, at every simulation step, instead of advancing the invadopodia in the absence of any ECM below the invadopodia, the invadopodia was advanced with the probability given by Eq. 4:

$$p_{\text{pen}} = 1.58 \times \left(1 - e^{-\text{LS}/100}\right). \quad (4)$$

Here, LS $(0 \leq \text{LS} \leq 100)$, or lateral stabilization, corresponds to the percentage of lateral invadopodia surface covered by ECM sites (Fig. 4 *A*). This description of p_{pen} models the influence of adhesion rings that surround the invadopodia and stabilize them (18). The prefactor 1.58 was chosen to ensure $p_{\text{pen}} \in (0, 1)$ (Fig. 4 *B*). At least 50 simulations per condition were performed, and information about ECM degradation and invadopodia speed was extracted from the data generated from these simulations. Although ECM degradation with feedback exhibited similar dependencies on ECM density and MMP secretion rate as before (Fig. 4 *C*), the dependency of invadopodia speed on MMP secretion rate was altered. Specifically, for the same ECM density, an increase in MMP secretion slowed down invadopodia growth by degrading the ECM, thereby reducing the extent of lateral support (Fig. 4 *D*).

Maintaining the aspect ratio of invadopodia structure, i.e., increasing invadopodia width as invadopodia penetrates inside the ECM, may enhance lateral stability of invadopodia. This enhanced lateral stability may in turn increase invadopodia speed. To test this possibility, simulations were performed with varying MMP secretion rates and ECM densities, where the width of the invadopodia was also increased as it penetrated into the ECM (Fig. S6 *A*; see Supporting Material for simulation details). The results were similar to those obtained for the previous case of fixed invadopodia width (i.e., aspect ratio changing continuously). However, for the same combination of ECM density and MMP secretion rate, ECM degradation was greater

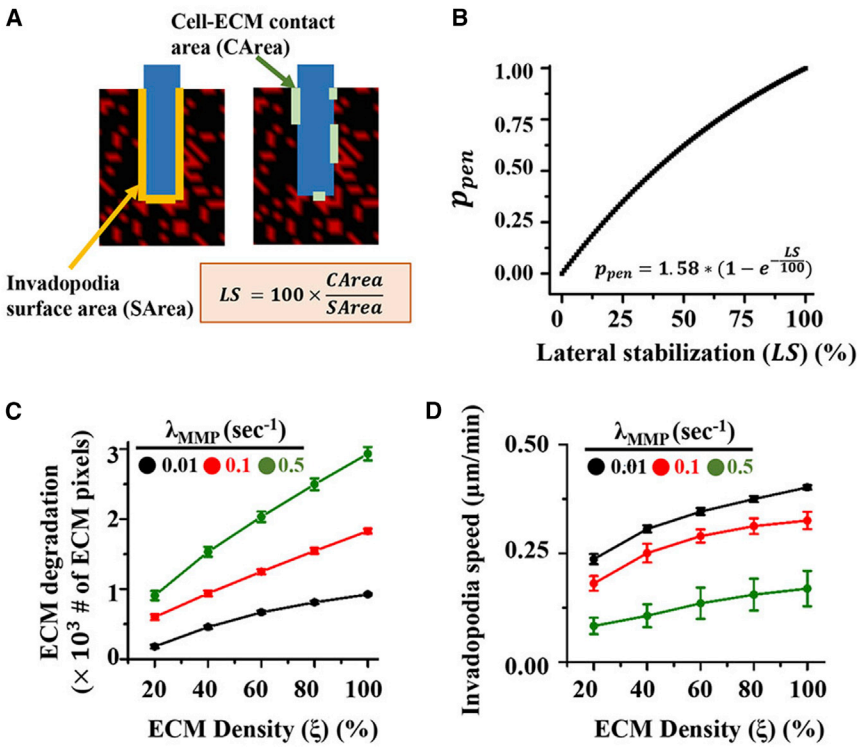

FIGURE 4 Effect of ECM-mediated lateral stabiization on ECM degradation and invadopodia speed. (*A*) To model the effect of cell-ECM adhesion on invadopodia penetration, the number of ECM sites surrounding the invadopodia structure was quantified and the probability of invadopodia penetration was made to depend on the fraction of lateral invadopodia surface covered by ECM sites. (*B*) Probability of penetration (p_{pen}) for varying extents of lateral stabilization. (*C* and *D*) Dependence of ECM degradation (*C*) and invadopodia speed (*D*) on ECM density, in the presence of cell-ECM adhesion-mediated feedback. At least 50 simulations per condition were performed. Error bars are ± standard deviation. To see this figure in color, go online.

when compared with the case where aspect ratio was changing (Fig. S6, *B* and *C*). Collectively, these results suggest that moderate MMP secretion rates ($\lambda_{MMP} = 0.1$ s^{-1} in our case) are required for striking a balance between ECM degradation and invadopodia penetration.

Inter-invadopodia spacing and MMP secretion rate collectively govern invasiveness of cancer cells

One interesting experimental observation was that in cells extending multiple invadopodia, the invadopodia were often clustered together in patches (Figs. 1 *A* and 5 *A*). A closer examination of the spatial positioning of these invadopodia revealed a dependence of inter-invadopodia spacing on ECM density. Specifically, the spacing between the nearest invadopodia decreased from $\sim$ 2.0 μm on 0.5% gelatin-coated substrates to $\sim$1.0 μm on 5.0% gelatin-coated substrates (Fig. 5, *A* and *B*). We hypothesize that inter-invadopodia spacing influences the invasiveness of cancer cells by modulating the connectivity of degraded zones created by individual invadopodia, with optimal inter-invadopodia spacing leading to fusion of these degraded zones. At high ECM densities, since instantaneous contact between ECM fibers and MMPs leads to exhaustion of the soluble MMP pool in the extracellular space, the spatial extent of lateral ECM degradation is restricted. Thus, fusion of adjoining degraded areas will require a closer inter-invadopodia spacing.

To test the above hypothesis, growth of two parallel invadopodia was simulated for three different values of inter-invadopodia spacing, i.e., $d = 1, 2, 3$ μm (Fig. 5 *C*; Movies S3 and S4). At least 50 simulations per condition were performed. For these simulations, the MMP secretion rate was chosen as moderate (i.e., $\lambda_{MMP} = 0.1$ s^{-1}) as it optimizes both ECM degradation and invadopodia penetration (Fig. 4, *C* and *D*). In addition to the total ECM degradation and invadopodia speed, pore size (quantified as the maximum surface area of the degraded region (Fig 5, *D* and E)) were also quantified. Independent of d, both ECM degradation (Fig. 5 *F*) and invadopodia speed (Fig. S7) increased in an ECM density-dependent manner. Although an increase in d enhanced ECM degradation at a given ECM density, at moderate and high ECM densities, both ECM degradation and invadopodia speed were maximal for $d \geq 2$ μm. In contrast to ECM degradation and invadopodia speed, pore size was nearly insensitive to ECM density and exhibited a biphasic dependence on d (Fig. 5 *G*), with maximum pore size observed at $d = 2$ μm, suggesting that optimal inter-invadopodia spacing maximizes ECM degradation and pore size. Lastly, since MMP secretion rate (λ_{MMP}) is expected to influence lateral ECM degradation, it may also influence size of pore(s) formed through ECM degradation. To study the collective influence of d and λ_{MMP} on ECM degradation and pore size, simulations were performed for $\lambda_{MMP} = 0.005$, 0.1, and 0.5 s^{-1} and $d = 1$, 2, and 3 μm (Fig. S8). As expected, for any given d, an increase in λ_{MMP} increased the total ECM degradation and pore size. However, for lowest MMP secretion rate, i.e., at $\lambda_{MMP} = 0.005$ s^{-1}, the largest pore size (*dotted yellow line*) was observed for $d = 1$ μm. Together, these results suggest that MMP secretion rate and inter-invadopodia spacing collectively regulate ECM degradation and pore size.

DISCUSSION

Invadopodia are actin-rich invasive structures that mediate cancer invasion through MMP-mediated ECM degradation. In this study, based on our experimental observations, we have developed a 3D computational model to probe how ECM density and cell-intrinsic MMP activity levels influence invadopodia activity and degrade ECM to create pores conducive to cell invasion. In addition to recapitulating ECM density-dependent increase in invadopodia activity and ECM degradation, we show that although invadopodia penetration is mediated by MT1-MMP activity, ECM degradation is mostly mediated by soluble MMPs. We then propose lateral stabilization as an important factor regulating invadopodia stability and demonstrate the need for tuning MMP secretion rates for achieving optimum penetration and ECM degradation. Finally, we extend this concept of lateral stabilization and demonstrate its importance with regards to inter-invadopodia spacing. Our results suggest that an optimum inter-invadopodia spacing maximizes the size of the pores created by ECM degradation (Fig. 6). Taken together, our results suggest that inter-invadopodia spacing and MMP secretion rates collectively regulate the size of the degraded areas created by invadopodia in an ECM density-dependent manner.

An increase in ECM stiffness, mediated by an increase in collagen density, has been correlated with increased cancer aggressiveness (49). Consistent with this finding, increased invadopodia-mediated ECM degradation was observed at the higher ligand density in MDA-MB-231 cells (Fig. 1), and was recapitulated by our computational model (Fig. 2). Although our experiments with the soluble MMP inhibitor SB-3CT are indicative of a dominant role for soluble MMPs in mediating ECM degradation (Fig. 3), complete suppression of ECM degradation by inhibition of MT1-MMP (Fig. S5) demonstrates its role in activating soluble MMPs, as has been previously reported (28,32,50). This is also captured by our model, whereby we observed a significant decrease in total ECM degradation when soluble MMP dynamics was switched off (Fig. 3).

Seminal work by Weaver and colleagues have demonstrated the direct influence of cell-matrix adhesions in supporting invadopodia maturation by enhancing protease activity (18). During 3D migration through fibrillar matrices, such support may be provided by surrounding

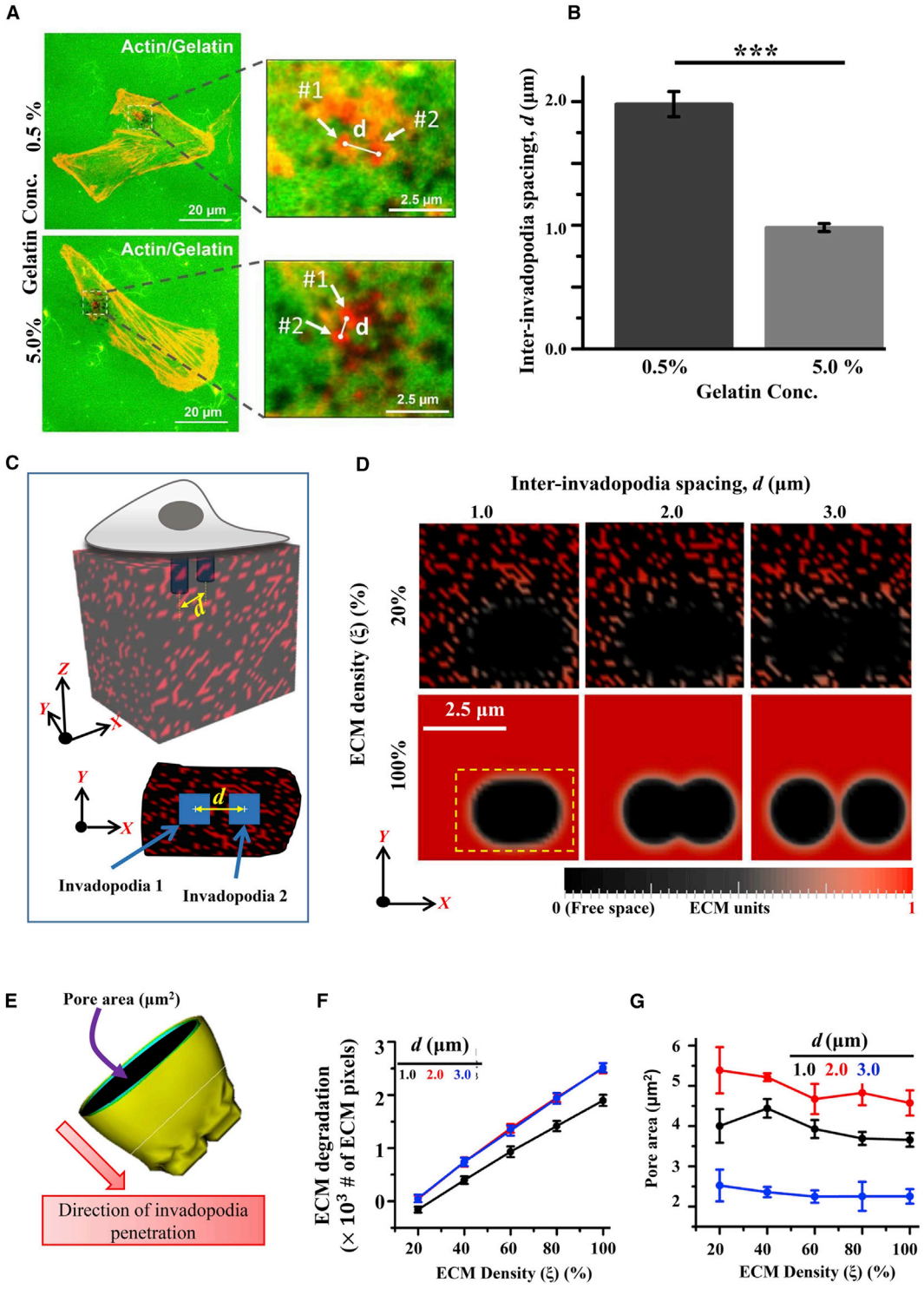

FIGURE 5 Inter-invadopodia spacing influences the size of invasion tracks. (*A*) Representative images of 1 μM Y-27632-treated MDA-MB-231 cancer cells cultured on 0.5 and 5.0% fluorescent gelatin. Scale bar represents 20 μm. Insets show colocalization of F-actin puncta and degraded areas. Scale bar represents 2.5 μm. (*B*) Quantitative analysis of inter-invadopodia spacing of Y-27632-treated MDA-MB-231 cancer cells cultured on 0.5 and 5.0% fluorescent gelatin. Only invadopodia spaced less than 5 μm apart were considered for quantification of inter-invadopodia spacing. Statistical significance was performed using one-way ANOVA ($n = 2$, 18–25 cells per condition; $^{***}p < 0.001$). Error bars show mean $\pm$ SE. (*C*) Multi-invadopodia simulations were performed where growth of two parallel invadopodia placed at a distance of $d = 1$, 2, and 3 μm was simulated. (*D*) Representative images showing size/shape of the degraded zones underneath the invadopodia at the end of the simulations for $d = 1$, 2, and 3 μm and for $\xi = 20$ and 100%. (*E*) Pore size was calculated as the area of the largest degraded region perpendicular to the direction of invadopodia penetration. Error bars are $\pm$ standard deviation. (*F* and *G*) ECM degradation and pore size for $d = 1$, 2, and 3 μm at varying ECM densities. Error bars are $\pm$ standard deviation. To see this figure in color, go online.

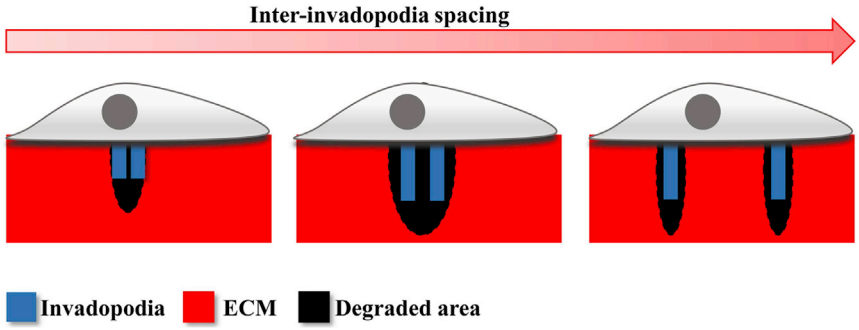

FIGURE 6 Tuning of inter-invadopodia spacing is required for maximizing size of degraded pores. Invadopodia-mediated ECM degradation creates ECM-free zones that work as invasion tracks for invading cells. Inter-invadopodia spacing (d) modulates size of invasion zones as well as degradation area. Although an increase in d results in increased degradation, the size of the largest pore created by invadopodia is maximal at moderate invadopodia spacing. To see this figure in color, go online.

ECM fibers (51). In such a case, high proteolytic degradation of the surrounding matrix may destabilize the invadopodia and negatively affect invasiveness. This effect is captured in our model, wherein an increase in MMP secretion rate leads to an increase in overall ECM degradation, but a reduction in invadopodia speed (Fig. 4). Instead, moderate MMP secretion rate is optimal for striking a balance between invadopodia penetration and total ECM degradation. Thus, for maximum invasiveness, cancer cells must possess regulatory mechanisms to modulate MMP activity in a manner that collectively optimizes ECM degradation and invadopodia stability.

Experiments with podosomes in 3T3 fibroblasts have revealed a dependence of inter-podosome spacing and podosome lifetime on substrate stiffness (52). Unlike podosomes, which cluster and form rosettes structures, invadopodia have not been shown to form such larger clusters. However, we do observe the presence of patches with closely spaced invadopodia. Interestingly, the inter-invadopodia spacing was found to exhibit ECM density dependence, with closer spacing at higher ECM density (Fig. 5). Through our computational results, we have established a link between inter-invadopodia spacing and cancer invasion by showing that inter-invadopodia spacing dictates the number and size of degraded pores, with maximal pore opening achieved at moderate inter-invadopodia spacing (Figs. 5 and 6). Although a lesser spread of MMPs was responsible for lower pore size at low inter-invadopodia spacing, pore size is limited at high inter-invadopodia spacing as MMP diffusion is not fast enough to fuse smaller pores formed far from each other (Fig. 5). Thus, collective tuning of inter-invadopodia spacing and MMP secretion rate can enhance invasiveness of cancer cells by facilitating the creation of pores big enough for enabling cancer cells to invade (Fig. S8). Also, given the relative insensitivity of pore formation to ECM density, ECM density-dependent tuning of MMP secretion rates may help to sustain invasion in an ECM density-independent manner.

In conclusion, based on our experimental findings, we have developed a 3D CA-based model for studying the collective influence of ECM density, cell-intrinsic MMP secretion rate, and inter-invadopodia spacing in influencing MT1-MMP and soluble MMP-mediated ECM degradation. Our results reveal the critical importance of inter-invadopodia spacing for creating pores that may support cancer invasion. Future work will focus on extending this model to incorporate invadopodia retraction (26), invadopodia dynamics in 3D settings, and studying the effect of ECM cross-linking (26). Although we have studied how lateral support-dependent feedback and inter-invadopodia spacing influence invadopodia activity, probing interdependence of these two quantities represents another direction for extending this work. Also, it remains unclear whether there exists any cross talk between microvesicles and invadopodia and whether invadopodia/MT1-MMP play any role in activation of microvesicles.

SUPPORTING MATERIAL

Supporting Materials and Methods, eight figures, and four movies are available at http://www.biophysj.org/biophysj/supplemental/S0006-3495(17)35039-7.

AUTHOR CONTRIBUTIONS

Conceived and designed the experiments, S.K., A.D., and S.S; Developed and executed the simulations, S.K; Performed the experiments, A.D. and A.B; Analyzed the data, S.K., A.D., and A.B; Wrote the manuscript, S.K., A.D., and S.S.

ACKNOWLEDGMENTS

We acknowledge the Industrial Research and Consultancy Centre for providing confocal microscopy and AFM facilities and the Indian Institute of Technology Bombay Computer Center for the computing facilities.

S.S. gratefully acknowledges financial support from Board of Research in Nuclear Sciences, India (grant 37(1)/14/02/2017-BRNS/37044), and from the Indian Institute of Technology Bombay. A.D. was financially supported by the Department of Biotechnology.

REFERENCES

1. Valastyan, S., and R. A. Weinberg. 2011. Tumor metastasis: molecular insights and evolving paradigms. *Cell.* 147:275–292.

2. Vanharanta, S., and J. Massagué. 2013. Origins of metastatic traits. *Cancer Cell.* 24:410–421.
3. Artym, V. V., Y. Zhang, …, S. C. Mueller. 2006. Dynamic interactions of cortactin and membrane type 1 matrix metalloproteinase at invadopodia: defining the stages of invadopodia formation and function. *Cancer Res.* 66:3034–3043.
4. Gimona, M., R. Buccione, …, S. Linder. 2008. Assembly and biological role of podosomes and invadopodia. *Curr. Opin. Cell Biol.* 20: 235–241.
5. Weaver, A. M. 2006. Invadopodia: specialized cell structures for cancer invasion. *Clin. Exp. Metastasis.* 23:97–105.
6. Weaver, A. M. 2008. Invadopodia. *Curr. Biol.* 18:R362–R364.
7. Linder, S., C. Wiesner, and M. Himmel. 2011. Degrading devices: invadosomes in proteolytic cell invasion. *Annu. Rev. Cell Dev. Biol.* 27:185–211.
8. Wolf, K., Y. I. Wu, …, P. Friedl. 2007. Multi-step pericellular proteolysis controls the transition from individual to collective cancer cell invasion. *Nat. Cell Biol.* 9:893–904.
9. Parekh, A., and A. M. Weaver. 2009. Regulation of cancer invasiveness by the physical extracellular matrix environment. *Cell Adhes. Migr.* 3:288–292.
10. Nishida, Y., H. Miyamori, …, H. Sato. 2008. Activation of matrix metalloproteinase-2 (MMP-2) by membrane type 1 matrix metalloproteinase through an artificial receptor for proMMP-2 generates active MMP-2. *Cancer Res.* 68:9096–9104.
11. Rosenblum, G., P. E. Van den Steen, …, I. Sagi. 2010. Direct visualization of protease action on collagen triple helical structure. *PLoS One.* 5:e11043.
12. Collier, I. E., W. Legant, …, G. I. Goldberg. 2011. Diffusion of MMPs on the surface of collagen fibrils: the mobile cell surface-collagen substratum interface. *PLoS One.* 6:e24029.
13. Hoshino, D., N. Koshikawa, …, K. Ichikawa. 2012. Establishment and validation of computational model for MT1-MMP dependent ECM degradation and intervention strategies. *PLoS Comput. Biol.* 8:e1002479.
14. Parekh, A., N. S. Ruppender, …, A. M. Weaver. 2011. Sensing and modulation of invadopodia across a wide range of rigidities. *Biophys. J.* 100:573–582.
15. Das, A., A. Kapoor, …, S. Sen. 2013. Extracellular matrix density regulates extracellular proteolysis via modulation of cellular contractility. *J. Carcinog. Mutagen.* S13:003.
16. Parekh, A., and A. M. Weaver. 2016. Regulation of invadopodia by mechanical signaling. *Exp. Cell Res.* 343:89–95.
17. Alexander, N. R., K. M. Branch, …, A. M. Weaver. 2008. Extracellular matrix rigidity promotes invadopodia activity. *Curr. Biol.* 18:1295–1299.
18. Branch, K. M., D. Hoshino, and A. M. Weaver. 2012. Adhesion rings surround invadopodia and promote maturation. *Biol. Open.* 1:711–722.
19. Beaty, B. T., V. P. Sharma, …, J. Condeelis. 2013. β1 integrin regulates Arg to promote invadopodial maturation and matrix degradation. *Mol. Biol. Cell.* 24:1661–1675, S1–S11.
20. Siqueira, A. S., M. P. Pinto, …, R. G. Jaeger. 2016. Laminin-111 peptide C16 regulates invadopodia activity of malignant cells through β1 integrin, Src and ERK 1/2. *Oncotarget.* 7:47904–47917.
21. Mueller, S. C., G. Ghersi, …, W.-T. Chen. 1999. A novel protease-docking function of integrin at invadopodia. *J. Biol. Chem.* 274: 24947–24952.
22. Anderson, A. R. 2005. A hybrid mathematical model of solid tumour invasion: the importance of cell adhesion. *Math. Med. Biol.* 22: 163–186.
23. Ramis-Conde, I., D. Drasdo, …, M. A. Chaplain. 2008. Modeling the influence of the E-cadherin-β-catenin pathway in cancer cell invasion: a multiscale approach. *Biophys. J.* 95:155–165.
24. Szabó, A., K. Varga, …, A. Czirók. 2012. Invasion from a cell aggregate–the roles of active cell motion and mechanical equilibrium. *Phys. Biol.* 9:016010.
25. Kumar, S., A. Kapoor, …, S. Sen. 2016. Proteolytic and non-proteolytic regulation of collective cell invasion: tuning by ECM density and organization. *Sci. Rep.* 6:19905.
26. Enderling, H., N. R. Alexander, …, A. M. Weaver. 2008. Dependence of invadopodia function on collagen fiber spacing and cross-linking: computational modeling and experimental evidence. *Biophys. J.* 95:2203–2218.
27. Saitou, T., M. Rouzimaimaiti, …, T. Suzuki. 2012. Mathematical modeling of invadopodia formation. *J. Theor. Biol.* 298:138–146.
28. Watanabe, A., D. Hoshino, …, K. Ichikawa. 2013. Critical role of transient activity of MT1-MMP for ECM degradation in invadopodia. *PLoS Comput. Biol.* 9:e1003086.
29. Martin, K. H., K. E. Hayes, …, S. A. Weed. 2012. Quantitative measurement of invadopodia-mediated extracellular matrix proteolysis in single and multicellular contexts. *J. Vis. Exp.* 66:e4119.
30. Kaewprag, J., W. Umnajvijit, …, M. Ponglikitmongkol. 2013. HPV16 oncoproteins promote cervical cancer invasiveness by upregulating specific matrix metalloproteinases. *PLoS One.* 8:e71611.
31. Gálvez, B. G., S. Matías-Román, …, A. G. Arroyo. 2001. Membrane type 1-matrix metalloproteinase is activated during migration of human endothelial cells and modulates endothelial motility and matrix remodeling. *J. Biol. Chem.* 276:37491–37500.
32. Murphy, D. A., and S. A. Courtneidge. 2011. The 'ins' and 'outs' of podosomes and invadopodia: characteristics, formation and function. *Nat. Rev. Mol. Cell Biol.* 12:413–426.
33. Swat, M. H., G. L. Thomas, …, J. A. Glazier. 2012. Multi-scale modeling of tissues using CompuCell3D. *Methods Cell Biol.* 110: 325–366.
34. Ahrens, J., B. Geveci, …, C. Johnson. 2005. 36-ParaView: an end-user tool for large-data visualization. The Visualization Handbook.
35. Sen, S., A. J. Engler, and D. E. Discher. 2009. Matrix strains induced by cells: computing how far cells can feel. *Cell. Mol. Bioeng.* 2:39–48.
36. Buxboim, A., I. L. Ivanovska, and D. E. Discher. 2010. Matrix elasticity, cytoskeletal forces and physics of the nucleus: how deeply do cells 'feel' outside and in? *J. Cell Sci.* 123:297–308.
37. Muralidharan-Chari, V., J. W. Clancy, …, C. D'Souza-Schorey. 2010. Microvesicles: mediators of extracellular communication during cancer progression. *J. Cell Sci.* 123:1603–1611.
38. D'Souza-Schorey, C., and J. W. Clancy. 2012. Tumor-derived microvesicles: shedding light on novel microenvironment modulators and prospective cancer biomarkers. *Genes Dev.* 26:1287–1299.
39. Schlienger, S., S. Campbell, and A. Claing. 2014. ARF1 regulates the Rho/MLC pathway to control EGF-dependent breast cancer cell invasion. *Mol. Biol. Cell.* 25:17–29.
40. Jerrell, R. J., and A. Parekh. 2016. Matrix rigidity differentially regulates invadopodia activity through ROCK1 and ROCK2. *Biomaterials.* 84:119–129.
41. Rosenberg, B. J., H. Gil-Henn, …, A. J. Koleske. 2017. Phosphorylated cortactin recruits Vav2 guanine nucleotide exchange factor to activate Rac3 and promote invadopodial function in invasive breast cancer cells. *Mol. Biol. Cell.* 28:1347–1360.
42. Pignatelli, J., D. A. Tumbarello, …, C. E. Turner. 2012. Hic-5 promotes invadopodia formation and invasion during TGF-β-induced epithelial-mesenchymal transition. *J. Cell Biol.* 197:421–437.
43. Muralidharan-Chari, V., J. Clancy, …, C. D'Souza-Schorey. 2009. ARF6-regulated shedding of tumor cell-derived plasma membrane microvesicles. *Curr. Biol.* 19:1875–1885.
44. Sedgwick, A. E., J. W. Clancy, …, C. D'Souza-Schorey. 2015. Extracellular microvesicles and invadopodia mediate non-overlapping modes of tumor cell invasion. *Sci. Rep.* 5:14748.
45. Sander, E. E., J. P. ten Klooster, …, J. G. Collard. 1999. Rac downregulates Rho activity: reciprocal balance between both GTPases

determines cellular morphology and migratory behavior. *J. Cell Biol.* 147:1009–1022.

46. Tsai, W.-C., C.-L. Chen, and H.-C. Chen. 2015. Protein tyrosine phosphatase SHP2 promotes invadopodia formation through suppression of Rho signaling. *Oncotarget.* 6:23845–23856.
47. Orgaz, J. L., P. Pandya, …, V. Sanz-Moreno. 2014. Diverse matrix metalloproteinase functions regulate cancer amoeboid migration. *Nat. Comm.* 5:4255.
48. Revach, O.-Y., A. Weiner, …, B. Geiger. 2015. Mechanical interplay between invadopodia and the nucleus in cultured cancer cells. *Sci. Rep.* 5:9466.
49. Levental, K. R., H. Yu, …, V. M. Weaver. 2009. Matrix crosslinking forces tumor progression by enhancing integrin signaling. *Cell.* 139: 891–906.
50. Sodek, K. L., M. J. Ringuette, and T. J. Brown. 2007. MT1-MMP is the critical determinant of matrix degradation and invasion by ovarian cancer cells. *Br. J. Cancer.* 97:358–367.
51. Tolde, O., D. Rösel, …, J. Brábek. 2010. The structure of invadopodia in a complex 3D environment. *Eur. J. Cell Biol.* 89:674–680.
52. Collin, O., P. Tracqui, …, E. Planus. 2006. Spatiotemporal dynamics of actin-rich adhesion microdomains: influence of substrate flexibility. *J. Cell Sci.* 119:1914–1925.